Article

ENDOR Studies of the Ligation and Structure of the Non-Heme Iron Site in ACC Oxidase

David L. Tierney, Amy M. Rocklin, John D. Lipscomb, Lawrence Que,, and Brian M. Hoffman

J. Am. Chem. Soc., **2005**, 127 (19), 7005-7013• DOI: 10.1021/ja0500862 • Publication Date (Web): 22 April 2005

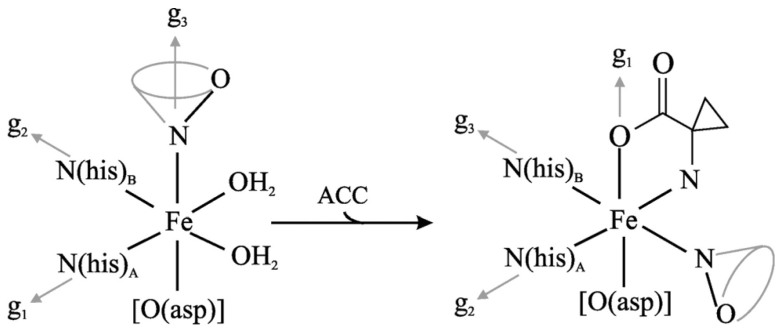

More About This Article

Additional resources and features associated with this article are available within the HTML version:

- Supporting Information
- Links to the 5 articles that cite this article, as of the time of this article download
- Access to high resolution figures
- Links to articles and content related to this article
- Copyright permission to reproduce figures and/or text from this article

View the Full Text HTML

J|A|C|S
ARTICLES
Published on Web 04/22/2005

ENDOR Studies of the Ligation and Structure of the Non-Heme Iron Site in ACC Oxidase

David L. Tierney,*,† Amy M. Rocklin,‡ John D. Lipscomb,*,‡ Lawrence Que, Jr.,*,§ and Brian M. Hoffman*,¶

Contribution from the Department of Chemistry, University of New Mexico, Albuquerque, New Mexico 87131, Department of Biochemistry, Molecular Biology and Biophysics and Department of Chemistry, University of Minnesota, Minneapolis, Minnesota 55455, and Departments of Chemistry and Biochemistry, Molecular Biology and Cell Biology, Northwestern University, Evanston, Illinois 60208

Received January 6, 2005; E-mail: dtierney@unm.edu

Abstract: Ethylene is a plant hormone involved in all stages of growth and development, including regulation of germination, responses to environmental stress, and fruit ripening. The final step in ethylene biosynthesis, oxidation of 1-aminocyclopropane-1-carboxylic acid (ACC) to yield ethylene, is catalyzed by ACC oxidase (ACCO). In a previous EPR and ENDOR study of the EPR-active Fe(II)−nitrosyl, [FeNO],[7] complex of ACCO, we demonstrated that both the amino *and* the carboxyl moieties of the inhibitor D,L-alanine, and the substrate ACC by analogy, coordinate to the Fe(II) ion in the Fe(II)−NO−ACC ternary complex. In this report, we use 35 GHz pulsed and CW ENDOR spectroscopy to examine the coordination of Fe by ACCO in more detail. ENDOR data for selectively ^{15}N-labeled derivatives of substrate-free ACCO−NO (**E-NO**) and substrate/inhibitor-bound ACCO−NO (**E-NO**−**S**) have identified two histidines as protein-derived ligands to Fe; ^{1,2}H and ^{17}O ENDOR of samples in D_2O and $H_2{}^{17}O$ solvent have confirmed the presence of water in the substrate-free Fe(II) coordination sphere (**E-NO**). Analysis of orientation-selective ^{14,15}N and ^{17}O ENDOR data is interpreted in terms of a structural model of the ACCO active site, both in the presence (**E-NO**−**S**) and in the absence (**E-NO**) of substrate. Evidence is also given that substrate binding dictates the orientation of bound O_2.

Ethylene is a plant hormone involved in all stages of growth and development, including regulation of germination, responses to environmental stress, and fruit ripening.[1] The commercial implications of these processes have made control of ethylene biosynthesis an attractive target for biochemical manipulation. The final step in ethylene biosynthesis, the O_2-coupled oxidation of 1-aminocyclopropane-1-carboxylic acid (ACC) to ethylene, CO_2, and HCN, is catalyzed by ACC oxidase (ACCO).[2−4]

ACCO possesses significant sequence homology to a number of structurally characterized non-heme Fe(II)-dependent oxygen-activating enzymes.[5] Indeed, a conserved His-X-Asp-$X_{(53-57)}$-His sequence is found among ACCOs that is equivalent to those in isopenicillin N synthase (IPNS),[6,7] deacetoxycephalosporin C synthase (DAOCS),[8] and the large family of 2-oxoacid-dependent dioxygenases.[9,10] The conserved His and Asp (or Glu) residues in this canonical sequence have been shown to bind Fe(II) in a ligand arrangement referred to as a "2-His-1-carboxylate facial triad".[5,11]

The cofactors necessary for ACCO catalysis (Fe(II), O_2, ascorbate, and CO_2)[12−16] are similar to those employed by the α-keto-acid-dependent dioxygenases (Fe(II), O_2, α-ketoglutarate), which first catalyze oxidative decarboxylation of α-ketoglutarate and then couple this process to the oxidation of substrate in the second part of the reaction.[9] Ascorbate in the ACCO reaction fulfills one of the roles of α-ketoglutarate in the dioxygenase reaction by supplying two of the electrons required for catalysis. However, ACCO appears to follow a

† University of New Mexico.
‡ Department of Biochemistry, Molecular Biology and Biophysics, University of Minnesota.
§ Department of Chemistry, University of Minnesota.
¶ Northwestern University.

(1) Reid, M. S. In *Plant Hormones and Their Role in Plant Growth and Development*; Davies, P. J., Ed.; Martinus Nijhoff Publishers: Dordrecht, The Netherlands, 1987; pp 257−279.
(2) Adams, D. O.; Yang, S. F. *Proc. Natl. Acad. Sci. U.S.A.* **1979**, *76*, 170−174.
(3) Hamilton, A. J.; Lycett, G. W.; Grierson, D. *Nature* **1990**, *346*, 284−287.
(4) Stella, L.; Wouters, S.; Baldellon, F. *Bull. Soc. Chim. Fr.* **1996**, *133*, 441−455.
(5) Costas, M.; Mehn, M. P.; Jensen, M. P.; Que, L., Jr. *Chem. Rev.* **2004**, *104*, 939−986.
(6) Roach, P. L.; Clifton, I. J.; Fulop, V.; Harlos, K.; Barton, G. J.; Hajdu, J.; Andersson, I.; Schofield, C. J.; Baldwin, J. E. *Nature* **1995**, *375*, 700−704.
(7) Roach, P. L.; Clifton, I. J.; Hensgens, C. M. H.; Shibta, N.; Schofield, C. J.; Hajdu, J.; Baldwin, J. E. *Nature (London)* **1997**, *387*, 827−830.
(8) Valegard, K.; Van Scheltinga, A. C.; Lloyd, M. D.; Hara, T.; Ramaswamy, S.; Perrakis, A.; Thompson, A.; Lee, H. J.; Baldwin, J. E.; Schofield, C. J.; Hajdu, J.; Andersson, I. *Nature* **1998**, *394*, 805−809.
(9) Prescott, A. G.; Lloyd, M. D. *Nat. Prod. Rep.* **2000**, *17*, 367−383.
(10) Borovok, H.; Landman, O.; Kreisberg-Zakarin, R.; Aharonowitz, Y.; Cohen, G. *Biochemistry* **1996**, *35*, 1981−1987.
(11) Hegg, E. L.; Que, L., Jr. *Eur. J. Biochem.* **1997**, *250*, 625−629.
(12) Ververidis, P.; John, P. *Phytochemistry* **1991**, *30*, 725−727.
(13) Brunhuber, N. M. W.; Mort, J. L.; Christoffersen, R. E.; Reich, N. O. *Biochemistry* **2000**, *39*, 10730−10738.
(14) Pirrung, M. C. *Acc. Chem. Res.* **1999**, *32*, 711−718.
(15) Rocklin, A. M.; Kato, K.; Liu, H.-w.; Que, L.; Lipscomb, J. D. *J. Biol. Inorg. Chem.* **2004**, *9*, 171−182.
(16) Thrower, J. S.; Blalock, R., III; Klinman, J. P. *Biochemistry* **2001**, *40*, 9717−9724.

catalytic cycle different from that of the dioxygenases, with ACC oxidation and O−O bond cleavage preceding reduction by ascorbate, which is proposed to come at the end of the reaction cycle.[15,17] The result is the production of ethylene and CO_2 and the release of both atoms of oxygen from O_2 as water rather than incorporation into the products, as in the case of the dioxygenases. Also, ACCO has a strict requirement for CO_2 as an activator, while it appears to be simply a product in the case of the dioxygenases.[15,16,18,19] Taken together, these results suggest that the Fe(II) center of ACCO may interact with substrates and effectors somewhat differently from the other structurally characterized members of the 2-His-1-carboxylate facial triad family.

In many cases, it has been shown that the 2-His-1-carboxylate facial triad environment is utilized to allow as many as three exogenous ligands to bind to Fe(II) in adjacent positions.[20−22] Nitric oxide has proven to be an effective probe of non-heme Fe(II) enzymes, converting the EPR silent Fe(II) center ($S = 2$) into the EPR active, $S = {}^3/_2$, $[FeNO]^7$ center.[23] The supposition that the non-heme iron site in ACCO is structurally similar to others containing the 2-His-1-carboxylate facial triad suggests that as many as two coordination positions in the NO complex might be occupied by additional exogenous ligands. In our initial EPR and ENDOR study of the Fe(II)−nitrosyl complex of ACCO,[17] we demonstrated that both the amino *and* the carboxyl moieties of the inhibitor D,L-alanine, and the substrate ACC by extension, coordinate to the Fe(II) ion in the Fe(II)−NO−Ala ternary complex. These results led to the new proposal for the mechanism of ethylene biosynthesis described above, in which the reaction begins with ACC and O_2 rather than ascorbate bound to the Fe(II).[17] This model received considerable support from our recent single turnover transient kinetic and product yield studies which showed that ethylene can be formed in the absence of ascorbate.[15] Recent CD/MCD studies of the enzyme in the absence of NO also support this model, showing that binding of ACC converts the iron center from six- to five-coordinate, leaving an open site for O_2 binding.[24] Ascorbate and CO_2 were shown to strongly influence the observed coordination number. Steady state kinetic studies also indicated an ordered ACC and O_2 binding reaction, but left in doubt whether ascorbate binds before or after this process in the reaction cycle.[16]

In this report, we use 35 GHz pulsed and CW ENDOR spectroscopy to characterize the ACCO coordination sphere in detail, through the study of substrate-free ACCO−NO (**E-NO**) and substrate/inhibitor-bound ACCO−NO (**E-NO−S/I**) prepared with various combinations of ^{14,15}NO, ^{14,15}N-D,L-alanine, ^{17}O-D,L-alanine, and $^{1,2}H_2O$,[16,17] using both ^{14}N (natural abundance) enzyme and enzyme grown on ^{15}N histidine. These measurements have corroborated the bidentate binding of substrates/inhibitors, identified two histidines as protein-derived ligands to Fe, and confirmed both the presence of at least one water ligand in **E-NO** and the lack of coordinated solvent in **E-NO−S**. Analysis of orientation-selective ^{14,15}N and ^{17}O ENDOR data provides a more detailed structural model of the ACCO iron active site than previously available from other techniques and suggests that the metal ligand site for O_2 is determined by the binding of substrate ACC.

Materials and Methods

All chemicals used were analytical grade or better (Sigma, Fisher, and Pharmacia) and were used without further purification. D_2O (99.9%) and L-histidine-(ring-$^{15}N_2$)·HCl·H_2O (98%) were purchased from Cambridge Isotope Laboratories, Inc.; $H_2{}^{17}O$ (39 and 52.8%) was purchased from Isotec, Inc.; ^{15}NO (99%) was purchased from ICON; ^{15}N-D,L-alanine (99%) was purchased from Sigma; ^{17}O-D,L-alanine was prepared as described previously.[17] Argon gas, used for anaerobic procedures, was passed over copper catalyst (BASF) at 170 °C to remove trace O_2. The BL21(DE3) histidine auxotroph was a generous gift from Dr. David A. Okar and Professor Alex J. Lange at the University of Minnesota. All protein concentrations were determined using the Sigma bicinchoninic acid protein assay[25] or estimated using the calculated molar extinction coefficient at 280 nm (27 550 M^{-1} cm^{-1}).

Growth, Overexpression, and Purification of ACCO. ACCO was expressed in *Escherichia coli* BL21(DE3)pLysS and purified as described previously.[17] The BL21(DE3) histidine auxotroph[26] was grown on the following minimal media, supplemented with either natural abundance L-histidine or $^{15}N_2$(ring)-L-histidine (25 mg/mL): 115 mM K_2HPO_4, 7.5 mM $(NH_4)_2SO_4$, 3.4 mM sodium citrate, pH 7.4, supplemented with 29.6 μM thiamine, 1% glucose, 0.2 mg/mL of ampicillin, 50 μM chloramphenicol, and Hutner's mineral base.[27] The enzyme used for these studies had a specific activity in the range of 2.9−3.5 mol ethylene per mol ACCO per minute.[17]

ENDOR Spectroscopy. Samples were prepared at 4 °C from deoxygenated stock solutions (repeated evacuation and replacement with Ar) using gastight syringes. All samples were prepared in 200 mM MOPS at pH 7.2, 10% glycerol, 50 mM $NaHCO_3$. Fe(II)ACCO was prepared by reconstitution of apo-ACCO with 0.8 molar equiv of ferrous ammonium sulfate. Samples in $H_2{}^{17}O$ were prepared by lyophilizing the enzyme at low temperature and reconstituting with $H_2{}^{17}O$ buffer. Control samples prepared in this fashion retained 98% of their original activity and yielded EPR and ENDOR spectra identical to those of the untreated enzyme. Samples containing either labeled or natural abundance ACC or alanine were prepared as described previously.[17] Samples in D_2O were prepared by dialyzing against 200 mM MOPS at pD 6.8, 10% glycerol, 50 mM $NaHCO_3$.

Q-band (35 GHz) ENDOR spectra were recorded with instruments of local design in either CW[28] or pulsed[29] mode. The CW spectra, unless otherwise noted, utilized the following conditions: 4 G field modulation (100 kHz); $T = 2$ K; $\nu_{MW} = 35.0$ GHz; MW power = 400 μW; time constant = 32 ms; RF power = 25 W (100 kHz bandwidth broadened); 1 MHz s^{-1} scan rate; receiver gain = 1000; 50 scans. Pulsed ENDOR spectra, unless otherwise noted, used the following conditions: $T = 2$ K; $\nu_{MW} = 34.70$ GHz; RF pulse length = 60 μs; (Davies) MW pulse

(17) Rocklin, A. M.; Tierney, D. L.; Kofman, V.; Brunhuber, N. M. W.; Hoffman, B. M.; Christoffersen, R. E.; Reich, N. O.; Lipscomb, J. D.; Que, L., Jr. *Proc. Natl. Acad. Sci. U.S.A.* **1999**, *96*, 7905−7909.
(18) Fernandez-Maculet, J. C.; Dong, J. G.; Yang, S. F. *Biochem. Biophys. Res. Commun.* **1993**, *193*, 1168−1173.
(19) Smith, J. J.; John, P. Maximizing the Activity of the Ethylene-Forming Enzyme. In *Cellular and Molecular Aspects of the Plant Hormone Ethylene*; Pech, J. C., Latche, A., Balague, C., Eds.; Kluwer Academic Publishers: Dordrecht, The Netherlands, 1993; pp 33−38.
(20) Arciero, D. M.; Orville, A. M.; Lipscomb, J. D. *J. Biol. Chem.* **1985**, *260*, 14035−14044.
(21) Arciero, D. M.; Lipscomb, J. D. *J. Biol. Chem.* **1986**, *261*, 2170−2178.
(22) Chen, V.; Orville, A. M.; Harpel, M. R.; Frolik, C. A.; Surerus, K. K.; Münck, E.; Lipscomb, J. D. *J. Biol. Chem.* **1989**, *264*, 21677−21681.
(23) Arciero, D. M.; Lipscomb, J. D.; Huynh, B. H.; Kent, T. A.; Münck, E. *J. Biol. Chem.* **1983**, *258*, 14981−14991.
(24) Zhou, J.; Rocklin, A. M.; Lipscomb, J. D.; Que, L., Jr.; Solomon, E. I. *J. Am. Chem. Soc.* **2002**, *124*, 4602−4609.
(25) Lowry, O. H.; Rosebrough, N. J.; Farr, A. L.; Randall, R. J. *J. Biol. Chem.* **1951**, *193*, 265−275.
(26) Okar, D. A.; Felicia, N. D.; Gui, L.; Lange, A. J. *Protein Expression Purif.* **1997**, *11*, 79−85.
(27) Cohen-Bazire, G.; Sistrom, W. R.; Stanier, R. Y. *J. Cell. Comput. Physiol.* **1957**, *49*, 25−68.
(28) Werst, M. W.; Davoust, C. E.; Hoffman, B. M. *J. Am. Chem. Soc.* **1991**, *113*, 1533−1538.
(29) Davoust, C. E.; Doan, P. E.; Hoffman, B. M. *J. Magn. Res. A* **1996**, *119*, 38−44.

lengths = 80, 40, and 80 ns; repetition rate = 50 Hz; 200 transients per point; (Re-Mims) τ = 140 ns; MW pulse lengths = 28, 28, 28, and 60 ns; repetition rate = 200 Hz; 500 transients per point.

For a single molecular orientation, the first-order ENDOR response from a nucleus with $I = {}^1/_2$ (e.g., ^{1}H, ^{15}N) is a doublet with frequencies $\nu_\pm = |{}^A/_2 \pm \nu_N|$, where A is the orientation-dependent hyperfine coupling, and ν_N is the nuclear Larmor frequency; for ${}^A/_2 > \nu_N$, this corresponds to a doublet centered at ${}^A/_2$ and split by $2\nu_N$, whereas for ${}^A/_2 < \nu_N$, it gives a doublet centered at ν_N and split by A. For nuclei with $I > {}^1/_2$, (e.g., ^{14}N, $I = 1$; ^{2}H, $I = 1$; ^{17}O, $I = {}^5/_2$), each peak of the doublet is further split into $2I$ lines, each separated by $3P$, with P being the orientation-dependent quadrupole coupling. Analysis of the nitrogen ENDOR data for ACCO was accomplished with the help of a series of selectively ^{15}N-labeled samples. In general, a ^{15}N substitution introduces a two-line pattern centered at $A(^{15}N)/2$, separated by $2\nu(^{15}N)$. This is accompanied by the loss of a corresponding four-line ^{14}N pattern, centered at $A(^{14}N)/2$, separated by $2\nu(^{14}N)$ and further split by $3P$ (see, for example, Figure 1). The ^{14,15}N patterns are further related by $A(^{15}N)/A(^{14}N) = \nu(^{15}N)/\nu(^{14}N) = g_N(^{15}N)/g_N(^{14}N) = 1.41$.

At the low- and high-field edges ("single-crystal-like" positions) of an EPR signal, an ENDOR experiment interrogates only a single molecular orientation or subpopulation; at intermediate fields, a well-defined subset of orientations is examined. Analysis of a 2D set of "orientation-selective" spectra collected at numerous fields across the EPR envelope often provides a complete determination of hyperfine and quadrupole interaction tensors.[30] As a first step in the analysis of the 2D (field frequency) ^{14,15}N ENDOR patterns for the various ACCO isotopologs, ^{14}N and ^{15}N ENDOR spectra, taken at the extrema (g_1 and g_3) of the $S = {}^3/_2$ [FeNO]^7 EPR signal, were compared and assigned (Figures 1−4). Simulations were then performed, with the initial goal of matching the ENDOR frequencies at g_1 and g_3, before finally being compared to the entire 2D field-frequency pattern (Figures 5, 6, and S5).

The observed EPR (and ENDOR) signals come from the $m_S = \pm{}^1/_2$ Kramers doublet of the $S = {}^3/_2$ spin manifold of the [FeNO]^7 adduct but are discussed in terms of an effective spin, with $S' = {}^1/_2$. As measured, a hyperfine tensor is referenced to the fictitious spin and is denoted $\mathbf{A}'$; its components are modified from those of the intrinsic tensor, denoted $\mathbf{A}$, in a well-defined way.[31] For example, when $\mathbf{g}$ and $\mathbf{A}$ are coaxial, $\mathbf{A}' = [A_1', A_2', A_3'] = [(g_1/g_e)A_1, (g_2/g_e)A_2, (g_3/g_e)A_3]$; the scaling by g_{obs}/g_e is more complicated for noncoaxial tensors, and this is included in simulations.[32] The quadrupole couplings are not scaled in this way.

The ^{15}N simulations faithfully reproduce the ^{15}N ENDOR frequencies over the entire range of fields (see, for example, Figure 5), giving reliable ^{15}N hyperfine tensors and orientations with respect to $\mathbf{g}$ (Table 2). In most cases, the corresponding ^{14}N patterns were not sufficiently resolved to warrant the same level of analysis. For clarity, specific isotopic substitutions are referred to (in parentheses) by the following conventions: **E-NO** = natural isotopic abundance, substrate-free ACCO−NO; **E**(^{15}N-His)**-NO** = substrate-free ACCO−NO, prepared from ^{15}N histidine-labeled enzyme; **E-**(^{15}**NO**) = substrate-free, natural abundance ACCO prepared with ^{15}NO; **E-NO−S** = natural abundance, ACC-bound ACCO−NO; **E**(^{15}N-His)**-NO−S** = ^{15}N histidine-labeled, ACC-bound ACCO−NO; **E-**(^{15}**NO**)**-S** = natural abundance, ACC-bound ACCO prepared with ^{15}NO; **E-NO−I**(^{15}N-Ala) = ^{15}N-D,L-alanine complex of natural abundance ACCO−NO; **E-NO−I**(^{17}O-Ala) = ^{17}O-D,L-alanine complex of natural abundance ACCO−NO. **E-NO−I** = natural abundance, D,L-alanine-bound ACCO−NO.

(30) Hoffman, B. M. *Acc. Chem. Res.* **1991**, *24*, 164−170.
(31) Hoffman, B. M.; DeRose, V. J.; Doan, P. E.; Gurbiel, R. J.; Houseman, A. L. P.; Telser, J. *EMR of Paramagnetic Molecules*. Plenum Press: New York, 1993; pp 151−218.
(32) Tierney, D. L.; Huang, H.; Martasek, P.; Roman, L. J.; Silverman, R. B.; Hoffman, B. M. *J. Am. Chem. Soc.* **2000**, *122*, 7869−7875.

Table 1. Single-Crystal-like Hyperfine and Quadrupole Couplings (MHz) at g_1 and g_3 for Ligand Atoms of **E-NO** and **E-NO−S**[a]

		A_1[b]	P_1[c]	A_3[d]	P_3[c]
		E-NO			
His_A	^{14}N (^{15}N)	(17)	nd	8 (12)	0.8
His_B	^{14}N (^{15}N)	(13)	nd	8 (12)	0.8
NO	^{14}N (^{15}N)	9 (12)	0.5	13 (20)	∼1
OH_2	^{17}O	≥20	nd	∼12	∼0.4
	^{2}H	1	∼0.3		
		E-NO−S			
His_A	^{14}N (^{15}N)	8 (11)	0.7	8 (12)	0.4
His_B	^{14}N (^{15}N)	7 (10)	0.4	10 (14)	0.6
NO	^{14}N (^{15}N)	10 (14)	0.7	12 (16)	0.3
ACC	^{14}N	6	0.9	7	0.4
Ala	(^{15}N)	(10)		(10)	
	^{17}O	14[e]	≤0.4	12	0.2
	$^{13}CO_2^-$ [f]	0.2[e]			

[a] The assignment of His_A and His_B for **E-NO** is not defined; the assignments for **E-NO−S** come from simulation of the full field-dependent datasets, as described in Figure 6 and Table 2. [b] Intrinsic hyperfine coupling at g_1: $A_1 = A_1'(g_e/g_1)$. [c] Quadrupole coupling in MHz (±0.1; "∼" ±0.2 MHz; nd = not determined). [d] Measured hyperfine coupling at g_3: $A_3 = A_3'$. [e] The signal was not detected at g_1. Value given is $A_2 = A_2'(g_e/g_2)$. [f] Data not shown.

Table 2. Hyperfine and Quadrupole Tensors (MHz) for Nitrogen Ligands of Fe^{II}-ACCO-NO ± ACC[a]

		A_{iso}	T	e_{T3}[a,b] θ, $\lvert\phi\rvert$	**P**(^{14}N)[c]
		E-NO			
His_A	^{15}N(^{14}N)	15 (11)	1.4 (1.0)	90, 20	
His_B	^{15}N(^{14}N)	14 (10)	1.4 (1.0)	90, 70	
NO	^{15}N(^{14}N)	16.5 (11)	3.3 (2.3)	25, 0	−0.2, −0.6, 0.8[d]
		E-NO−S			
His_A	^{15}N	11	1.6	0, 0	
His_B	^{15}N	13	1.6	90, 90	
NO	^{15}N(^{14}N)	15 (11)	2.0 (1.4)	25, 0	−0.4, −0.7, 1.1[d]
Ala	^{15}N	11.5	1.6	90, 90	
ACC	^{14}N	8	1.0	90, 90	−0.4, 1.1, −0.7

[a] The hyperfine tensors were modeled as a sum of isotropic (A_{iso} (MHz)) and axial anisotropic ($\mathbf{T} = [-T, -T, +2T]$ (MHz)) contributions. The orientation of the unique direction of the anisotropic coupling is denoted e_{T3}. [b] Euler angles describing the orientation of e_{T3} (see footnote a): θ = angle between g_3 and e_{T3} (±10°); $|\phi|$ = angle of rotation about g_3 (±30°). [c] Quadrupole tensor, $\mathbf{P} = [P_1, P_2, P_3]$ (MHz). [d] Angles between the principal quadrupole and hyperfine axes (α, β) = (25°, 0°).

Results

As previously reported, the addition of NO to Fe(II)−ACCO leads to the formation of an $S = {}^3/_2$ [FeNO]^7 adduct (**E-NO**) with a nearly axial EPR spectrum ($g_{1,2,3}$ = [4.11, 3.94, 1.99]; E/D = 0.008; Figure S1).[17] Inclusion of substrate ACC or an amino acid inhibitor, such as alanine, leads to the formation of an **E-NO−S/I** complex whose EPR spectrum is more rhombic ($g_{1,2,3}$ = [4.23, 3.82, 1.99]; E/D = 0.035) than that of **E-NO**. The resulting complex also requires 10-fold less microwave power to effect half-saturation ($P_{1/2}$). Complexes with substrate analogues that contain either a carboxyl or an amino function, but not both, yield EPR spectra that are similar in appearance to that of **E-NO**, although their power saturation behavior is closer to that of the ACC complex. ^{14,15}N and ^{17}O ENDOR at 35 GHz were used previously to demonstrate that both the amino and carboxy functions of ACC coordinate the active site Fe(II) simultaneously in the ternary ACCO−NO−ACC complex.[17] In the current study, we have isotopically labeled all of the nuclei directly coordinated to the metal ion, save the putative protein-derived carboxylate.

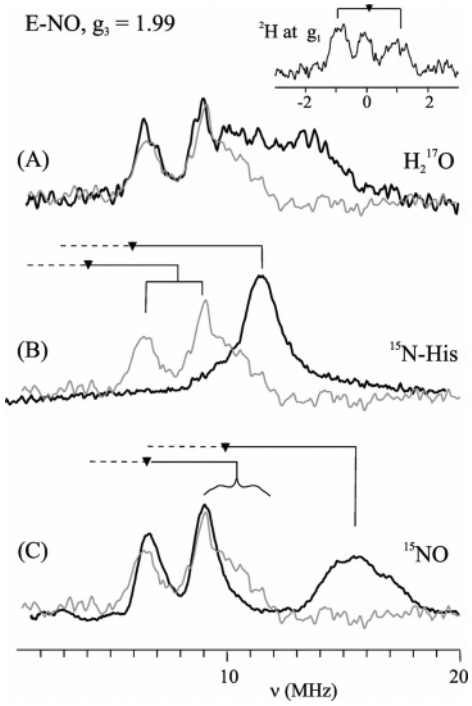

Figure 1. The 35 GHz CW ENDOR of ACCO−NO (**E-NO**) at $g_3 = 1.99$. (A) **E-NO** in 42% $H_2{}^{17}O$ buffer. Inset: 35 GHz Re-Mims ^2H ENDOR of a sample in D_2O buffer at $g_1 = 4.11$. (B) ^{15}N-His. (C) ^{15}NO. The corresponding natural abundance spectrum is overlayed as a gray line in each trace for comparison. The brackets are included to guide the eye, where the inverted triangle represents $A'(^{14,15}N)/2$.

The 35 GHz CW ENDOR spectra from this suite of samples exhibit the ν_+, but not the ν_-, branches for coordinated ^{17}O and $^{14,15}N$. Although this is a common phenomenon, its origin is not understood. In contrast, the Davies-pulsed ENDOR spectra contain both branches for $^{14,15}N$. As will be seen, overlap between ν_- from one nitrogen with ν_+ from another can interfere with the analysis of individual spectra. In general, pulsed ENDOR spectra were considerably sharper than CW spectra at g_1 and at fields around g_2 (see, for example, Figure 4, traces D and E), but the signals were difficult to observe at intermediate fields. At fields near $g_3 = 1.99$, pulsed ENDOR could not be obtained because of the presence of an extraneous EPR signal, presumably from nonspecifically bound NO. However, reliable data could be obtained at g_3 in CW mode (Figures 1 and 3) by moving to fields sufficiently high that any contributions from the minority species were eliminated. The greater sensitivity of the CW technique also afforded spectra at fields intermediate to g_2 and g_3, allowing the field-dependence of the $^{14,15}N$ patterns to be determined. In short, the detailed analysis presented here was made possible through combined application of CW and pulsed techniques.

We begin with a presentation of "single-crystal-like" ENDOR spectra taken at g_1 and g_3 for **E-NO** (one fewer nitrogen ligand, below), followed by the equivalent ENDOR spectra for **E-NO−S/I**; we then discuss the analysis of 2D field-frequency data.

Single-Crystal-Like ENDOR of E-NO: Water Coordination. The presence of Fe-bound water in **E-NO** is established by the ENDOR results for a sample prepared without substrate in $H_2{}^{17}O$. At the high-field edge of the **E-NO** EPR signal ($g_3 = 1.99$; Figure 1A), the natural abundance 35 GHz CW ENDOR spectrum ($H_2{}^{16}O$, gray line) consists of sharp resonances at ∼7 and 9 MHz and a broad component at ∼10 MHz; all are attributed to coordinated ^{14}N (discussed below). These same features are present in spectra for a sample prepared in $H_2{}^{17}O$ buffer, with the addition of a broad resonance from ^{17}O, located at $\nu_+(^{17}O) \sim 13$ MHz (black line, Figure 1A). The relationship, $\nu_+(^{17}O) = A(^{17}O)/2 + \nu(^{17}O)$, gives $A_3(^{17}O) \sim 12$ MHz. This signal was difficult to observe at fields below $g \sim 2.8$, due in part to increasing overlap with resonances from strongly coupled ^1H (see Figure 2, inset), but also because of a monotonic increase in the apparent width of the signal at increasingly lower fields (Figure S2). The observation of an ^{17}O signal with a value of $A(^{17}O)$ this large requires the presence of at least one water molecule in the coordination sphere of substrate-free ACCO−NO. The width of the ^{17}O resonance may include sizable contributions from structural heterogeneity, such as the presence of multiple discrete orientations for a single coordinated water, or, alternatively, from two simultaneously coordinated water molecules.

The presence of exchangeable protons associated with the bound water was confirmed with 35 GHz refocused-Mims (Re-Mims)[33] pulsed ^2H ENDOR of a sample of **E-NO** in D_2O buffer ($g_1 = 4.11$, Figure 1, inset). The Re-Mims protocol allows the use of short τ, independent of spectrometer deadtime (τ is the delay between the first and second microwave pulses of Mims pulsed ENDOR[34]), which diminishes the ENDOR response of weakly coupled and matrix ^2H and favors signals from more strongly coupled ^2H. The spectrum shows a ^2H doublet split by $A_1'(^2H) \sim 2$ MHz, corresponding to a ^1H coupling of $A'_H \sim 13$ MHz ($g_H/g_D = 6.5$), or an intrinsic value, $A_H \sim 6.5$ MHz ($g_{obs}/g_e \sim 2$). This coupling is compatible with that expected for the protons of the bound solvent whose presence is indicated by the ^{17}O species identified in Figure 1A. The ^2H ENDOR response attenuates rapidly for $g < 3.8$, precluding field-dependent analysis. This example illustrates the importance of using multiple ENDOR techniques. The signal from the exchangeable water protons was not detected in the CW ^1H ENDOR spectra of **E-NO**. At nearly all fields, the ^1H ENDOR is dominated by several moderately strongly coupled, non-exchangeable proton signals ($A' \sim 8-18$ MHz, intrinsic $A \sim 4-9$ MHz), which likely arise from Fe-bound histidyl imidazoles (discussed below).

E-NO Nitrogen Ligands: E(^{14,15}N-His)-NO. Comparison of the spectra for natural abundance **E-NO** and **E**(^{15}N-His)-**NO** (Figure 1B; gray and black lines, respectively, $g_3 = 1.99$) shows that the two sharp ^{14}N features in the former spectrum (at ∼7 and 8 MHz) are lost upon ^{15}N histidine incorporation, while a single new peak appears at ∼12 MHz. The broad component near 10 MHz in the natural abundance spectrum is unaffected and, as shown presently, can be attributed to ^{14}N from coordinated NO. The correspondence between the frequencies in the two spectra establishes that the two sharp lines in the ^{14}N spectrum are the ν_+ quadrupole doublet of a single *type* of histidyl imidazole.

The $g_1 = 4.11$ CW spectrum of natural abundance **E-NO** contains overlapping signals from strongly coupled ^{14}N and ^1H in the range of 1−40 MHz (Figure 2, inset). CW ENDOR spectra from **E**(^{15}N-His)-**NO** (black line in Figure 2A) show two ^{15}N peaks at ∼16 and ∼20 MHz that are absent without the label (gray line in Figure 2A). As they are separated by

(33) Doan, P. E.; Hoffman, B. M. *Chem. Phys. Lett.* **1997**, *269*, 208−214.
(34) Mims, W. B. *Proc. Royal Soc. London* **1965**, *A283*, 452−457.

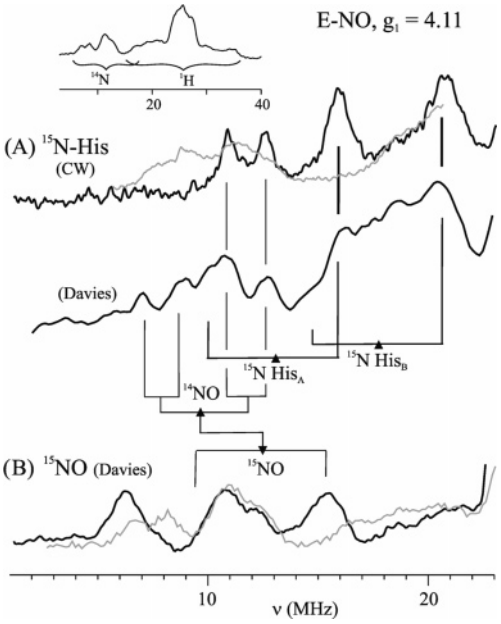

Figure 2. The 35 GHz CW and Davies-pulsed ENDOR of substrate-free ACCO−NO (**E-NO**) at $g_1 = 4.11$. (A) (top) CW spectra for **E(**^{14,15}**N-His)-NO**; (bottom) Davies spectrum for **E(**^{15}**N-His)-NO**. (B) Davies spectra for **E-(**^{15}**NO)**. Natural abundance spectra are overlayed in gray for comparison. Inset: 35 GHz Davies-pulsed ENDOR of natural abundance ACCO−NO at $g_1 = 4.11$, showing strong overlapping signals from ^{14}N and ^{1}H.

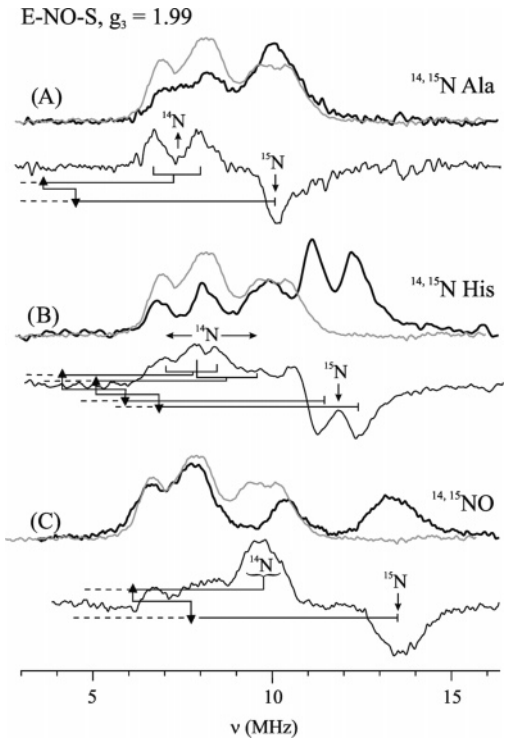

Figure 3. The 35 GHz CW ENDOR of ACCO−NO + ACC/Ala (**E-NO−S/I**) taken at $g_3 = 1.99$. (A) ^{15}N Ala. (B) ^{15}N-His. (C) ^{15}NO. The natural abundance spectrum is overlayed as a gray line for comparison, and (^{14}N) − (^{15}N) difference spectra are displayed below each dataset.

less than $2\nu(^{15}\text{N})$, they must be the ν_+ features for two magnetically distinct ^{15}N-His coordinated to Fe.[35] Thus, the single type of ^{15}N seen in the $g_3 = 1.99$ spectrum resolves into two distinct ^{15}N-His, denoted A and B, at $g_1 = 4.11$.

The **E**(^{15}N-His)-**NO** CW spectrum also shows a pair of lines at ∼11 and 13 MHz that are not resolved in the natural abundance **E-NO** spectrum. Their appearance in the ^{15}N-His spectrum suggests that they too are ^{15}N features. However, their frequencies do not correspond with those expected for $\nu_-(^{15}\text{N})$. Comparison with the 35 GHz Davies-pulsed ENDOR spectrum (Figure 2A) shows that the pair should be assigned to the ν_+ quadrupole pair of ^{14}NO. The Davies spectrum contains strong ν_+ resonances for the two ^{15}N-His at ∼16 and ∼20 MHz, weak features that correspond to the two $\nu_-(^{15}\text{N})$ resonances, and all four resonances from ^{14}NO, as indicated by the brackets in Figure 2. These assignments are supported by the Davies-pulsed ENDOR of **E-(**^{14,15}**NO)** (discussed below), as summarized in Table 1.

E-NO Nitrogen Ligands: E-(^{14,15}**NO).** The broad shoulder from ∼9.5−12 MHz in the $g_3 = 1.99$ CW spectrum of natural abundance **E-NO** (Figure 1C) is eliminated in the ENDOR spectrum of **E-(**^{15}**NO)** (black line, Figure 1C), and its disappearance is accompanied by the appearance of a new ^{15}N resonance at ∼15 MHz. The ENDOR frequencies, as indicated by the brackets, match such that the ^{14}N shoulder at ∼10 MHz in natural abundance enzyme (Figure 1A,B) and the ^{15}N resonance at 15 MHz in Figure 1C indeed come from the ν_+ branches of ^{14,15}NO. The ^{14}NO quadrupole coupling at g_3 could only be estimated from the breadth of the ^{14}NO feature; it is included in Table 1, along with the hyperfine constants.

Comparison of the $g_1 = 4.11$ Davies ENDOR spectra of **E-(**^{15}**NO)** and **E-NO** (Figure 2B, black line and gray line, respectively) shows that the ^{14}NO → ^{15}NO substitution introduces a new feature at ∼15 MHz and causes the loss of the intensity from the corresponding $\nu_-(^{14}\text{NO})$ doublet at ∼7−9 MHz. Comparison of Figure 2B to the Davies ENDOR of **E**(^{15}N-His)-**NO** in Figure 2A indicates that the pair of lines at ∼11 and 13 MHz in Figure 2A are indeed the ν_+ quadrupole doublet of ^{14}NO. This doublet is surprisingly sharp, possibly reflecting the lack of underlying ν_+ and ν_- resonances from ^{14}N-His. Resonances from $\nu_+(^{14}\text{N-His})$ dominate the CW spectrum, effectively masking any intensity differences associated with the loss of $\nu_+(^{14}\text{NO})$.

Single-Crystal-Like ENDOR of E-NO−S/I: E-NO−S/I Coordinated Oxygen. Spectra from **E-NO−S** samples prepared in $H_2{}^{17}O$ solvent did not show signals from ^{17}O, indicating an absence of coordinated water. Likewise, no solvent exchangeable ^{1}H ENDOR signals, either from coordinated water or from the amine nitrogens of substrate/inhibitor, could be detected for **E-NO−S/I** complexes. ^{17}O ($I = {}^5/_2$) incorporated in the carboxyl oxygens of D,L-alanine used to form the **E-NO−I** complex gives an intense ν_+ (^{17}O) ENDOR feature from a strongly coupled ^{17}O; at $g_3 = 1.99$, the signal is particularly well defined, with $A_3(^{17}\text{O}) \approx 0.12$ MHz (Figure S3). This large ^{17}O hyperfine coupling requires that the carboxylate group of alanine be coordinated to the iron center.[17]

E-NO−S/I Coordinated Nitrogens: E-NO−S. The CW spectra at $g_3 = 1.99$ from the suite of **E-NO−S** ^{14,15}N isotopologs exhibit the ν_+, but not the ν_-, branches for coordinated ^{14,15}N (Figure 3). To best visualize the effects of individual isotopic substitutions, (^{14}N) − (^{15}N) difference spectra were calculated; these are shown directly below the experimental data in Figure 3. The difference spectra were calculated to minimize baseline deviations to low- and high-frequency of the

(35) Although there are strongly coupled proton signals in this frequency region, they are poorly resolved and merely contribute a background signal.

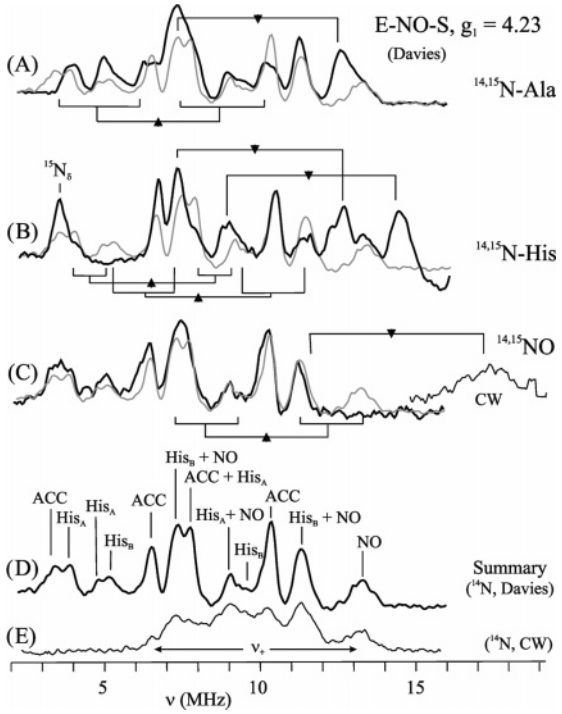

Figure 4. The 35 GHz Davies-pulsed ENDOR of substrate-bound ACCO−NO (**E-NO−S/I**) at $g_1 = 4.23$. In traces A−C, the natural abundance ^{14}N spectrum is shown as a gray line. (A) ^{15}N−Ala. (B) ^{15}N−His. (C) ^{15}NO. Inset: CW detection of $\nu_+(^{15}\text{NO})$. (D) Summary of assignments for natural abundance ACCO−NO + ACC at $g_1 = 4.23$. (E) The 35 GHz CW spectrum of natural abundance **E-NO−S** showing the expected intensity pattern for $\nu_+(^{14}\text{N})$.

signals of interest and are, therefore, purely qualitative. Such (^{14}N) − (^{15}N) difference spectra will show a single negative feature for each ^{15}N and (in principle) two positive features for the corresponding ^{14}N. The $g_1 = 4.23$, Davies-pulsed ENDOR spectra from this suite show both ν_+ and ν_- ^{14,15}N features and are extraordinarily sharp and richly detailed (Figure 4).

E-NO−S/I Coordinated Nitrogens: E-NO−I(^{14,15}N-Ala). The $g_3 = 1.99$ 35 GHz CW ENDOR spectrum of **E-NO−I**(^{15}N-Ala) (black line in Figure 3A) shows a subtle change from the natural abundance **E-NO−I** spectrum (gray line, Figure 3A) that is best visualized by examination of the (^{14}N-Ala) − (^{15}N-Ala) difference spectrum. This displays a pair of positive peaks from the ν_+ quadrupole pair of coordinated ^{14}N-Ala (centered at $A(^{14}\text{N-Ala})/2 + \nu(^{14}\text{N})$[36] and split by $3P = 1.2$ MHz) and a single negative feature from ^{15}N-Ala (centered at $A(^{15}\text{N-Ala})/2 + \nu(^{15}\text{N})$). The associated hyperfine couplings are related by $A(^{15}\text{N})/A(^{14}\text{N}) = 1.4$ as required. These couplings, along with those at g_3, are summarized in Table 1.

The 35 GHz $g_1 = 4.23$ Davies-pulsed ENDOR spectrum of **E-NO−I**(^{15}N-Ala)[17] (Figure 4A) clearly shows the gain of ^{15}N features at ∼7 and 13 MHz (black line) and the loss of ^{14}N signals at ∼3 and 10 MHz (gray line). The braces above the spectra show the assignment of the 8 and 13 MHz features as the ν_- and ν_+ branches of ^{15}N from alanine; those below the spectra show the corresponding assignment of the 3 and 10 MHz ^{14}N features. The values of A and P are given in Table 1.

E-NO−S/I Coordinated Nitrogens: E(^{14,15}N-His)-NO−S. The $g_3 = 1.99$ CW spectrum of **E**(^{15}N-His)-**NO−S** collected at g_3 (black line, Figure 3B) shows two intense $\nu_+(^{15}\text{N})$ features at ∼11 and 12 MHz, as highlighted in the difference spectrum. The separation of these two peaks is much less than $2\nu(^{15}\text{N})$, indicating that they arise from two magnetically distinct ^{15}N-His ligands. The appearance of the two new features in the ^{15}N-His spectrum is accompanied by a reduction in intensity of the ^{14}N peaks near 7 and 8 MHz, visualized as positive features in the (^{14}N) − (^{15}N) difference spectrum; tentative ^{14}N assignments are indicated by the brackets.

The $g_1 = 4.23$ Davies ENDOR spectrum of **E**(^{15}N-His)-**NO−S** (Figure 4B) also shows $\nu_+(^{15}\text{N})$ features at ∼13 and 15 MHz from the two histidine ligands; corresponding $\nu_-(^{15}\text{N})$ features at ∼8 and 10 MHz are indicated by the brackets. Although there is a clear loss of ^{14}N-His intensity at ∼5, 8, and 12 MHz, quadrupole splittings are not clearly resolved; as indicated by the braces, we estimate $3P_A \approx 1.1$ and $3P_B \approx 2.0$ MHz. An additional feature at $\nu(^{15}\text{N}) = 3.5$ MHz in the ^{15}N-His spectrum can be attributed to unresolved $^{15}\text{N}_\delta$ of labeled histidine.

E-NO−S/I Coordinated Nitrogens: E-(^{14,15}NO)−S. Comparison of the $g_3 = 1.99$ CW ENDOR spectra for **E-**(^{15}**NO**)**−S** and **E-NO−S** (Figure 3C) shows the loss of a broad $\nu_+(^{14}\text{N})$ feature at ∼10 MHz and the gain of a $\nu_+(^{15}\text{N})$ feature at ∼13 MHz. These frequencies give $A_3'(^{15}\text{NO}) \approx 16$ MHz and $A_3'(^{14}\text{NO}) \approx 12$ MHz; the ^{14}N quadrupole splitting is unresolved at this field, but the breadth of the ^{14}N feature suggests that $3P_3 \approx 0.9$ MHz. We attribute the breadth of the ^{14,15}NO feature to a distribution of geometries from rotation about the Fe−N(NO) bond.

There is little difference between the $g_1 = 4.23$ Davies ENDOR spectra for **E-**(^{15}**NO**)**−S** and that for **E-NO−S** (black and gray lines, respectively, in Figure 4C), except for the loss of ^{14}N intensity at ∼13 MHz. Examination of the ^{15}N-His spectrum (black line in Figure 4B), in which resonances from ^{14}NO are unaffected, suggested the quadrupole partner to this peak might be at ∼11 MHz. Assignment of this ^{14}N pair as the quadrupole split $\nu_+(^{14}\text{NO})$ doublet predicts the pattern indicated by the ^{15}N upper brackets in Figure 4C, with the ν_+ resonance of ^{15}NO at ∼17 MHz. This ^{15}N feature is not detected in Davies ENDOR of **E-**(^{15}**NO**)**−S**, but it is detected in CW mode (inset to Figure 4C, labeled "CW"). This observation confirms the assignment and again illustrates the importance of employing both CW and pulsed ENDOR in the confirmation of frequency assignments.

E-NO−S, g_1 Summary. The resulting assignment of features in the ^{14}N Davies ENDOR spectrum of natural abundance **E-NO−S** at $g_1 = 4.23$ is summarized in Figure 4D and accounts for all 16 resonances expected for four ^{14}N ligands: eight lines from two distinct histidines, four from the amine nitrogen of substrate, and four from the nitrogen of NO. Examination of Figure 4D shows some intensity anomalies in the Davies spectrum, particularly in the region around 9−10 MHz. Although the origin of the intensity differences is not clear, this is the area of greatest spectral congestion. The corresponding 35 GHz CW ENDOR spectrum (Figure 4E), which only includes contributions from $\nu_+(^{14}\text{N})$ (above), shows no peaks below ∼7 MHz, consistent with the assignments in Figure 4D. Interestingly, the CW spectrum displays an intensity pattern more consistent with that predicted by the Davies ENDOR than does the Davies spectrum itself.

(36) At this magnetic field, $A(^{14}\text{N}) = 3.8$ MHz and $A(^{15}\text{N}) = 5.4$ MHz.

Scheme 1

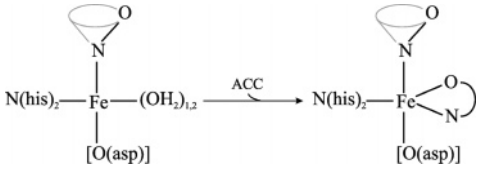

Orientation-Selective ^{15}N ENDOR. The preceding sections describe the nitrogen ENDOR at g_1 and g_3 and deduce A and P values at these single-crystal-like positions. This information is summarized in Scheme 1. To obtain more detailed structural information, CW ENDOR data were collected at fields across the entire EPR envelope for all of the isotopologs, both with and without substrate. Analysis of these 2D field-frequency plots to obtain hyperfine and quadrupole tensors is simplified because only ν_+ resonances are observed in CW mode. Two representative 2D field-frequency plots, one for **E**(^{15}N-His)-**NO** (Figure 5) and one for **E**(^{15}N-His)-**NO**−**S** (Figure 6), are shown. The remaining datasets [**E**-(^{15}**NO**), **E-NO**−**I**(^{15}N-Ala), and **E**-(^{15}NO)-**S**] are included as Supporting Information (Figures S6−S8). The greater rhombicity of the **E-NO**−**S/I** EPR signal (E/D = 0.035) gives greater field dispersion to the ENDOR patterns and results in sharper ENDOR lines, particularly near g_2 (compare Figures 5 and 6). This affords increased precision in the geometric parameters derived from simulations, especially the angle ϕ which corresponds to the rotation of the hyperfine tensor frame about the g_3 axis. Resultant hyperfine tensors, obtained as described below, are given in Table 2.

E-NO. The hyperfine tensor for a ^{14,15}N of histidine coordinated to Fe is essentially axial, with $A_{||} > A_\perp$ and $A_{||}$ along the Fe−N bond. The data shown above (Figure 3B) demonstrate that the A and B histidyl nitrogens are magnetically equivalent in spectra taken at g_3. We take the equivalence of N_A and N_B at g_3 to indicate that $A(g_3) \approx A_\perp$ and that g_3 is roughly normal to the plane defined by the Fe and the two Fe−N (His) bonds; as a result, A_2 will lie in the g_1−g_2 plane. This was used as the starting point to simulate the 2D patterns of ν_+(^{15}N) features from histidine; Figure S5 highlights the ^{15}N features by overlaying the **E**(^{15}N-His)-**NO** with the natural abundance **E-NO** spectra. The best simulations are shown in Figure 5; the solid lines drawn through the simulations represent the tensor components that connect g_1 to g_2 and g_1 to g_3 and are included to guide the reader. The tensor components for $^{15}N_A$ and $^{15}N_B$ are essentially the same, with the best interpretation of the angles being that the two Fe−N bonds (A_2) are at roughly right angles to each other in the g_1−g_2 plane, with one along g_2 and the other along g_1.

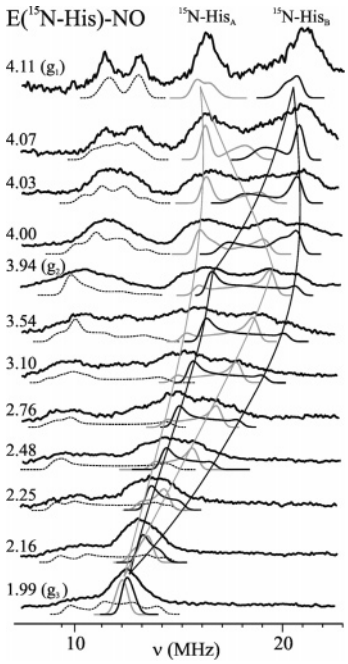

Figure 5. Field-dependent ^{15}N 35 GHz CW ENDOR of **E(^{15}N-His)-NO**. Fields are as indicated on the plot. Representative simulations, summarized in Table 2, are shown as: gray = ^{15}N-His$_A$, black = ^{15}N-His$_B$, black, long dash = ^{14}NO.

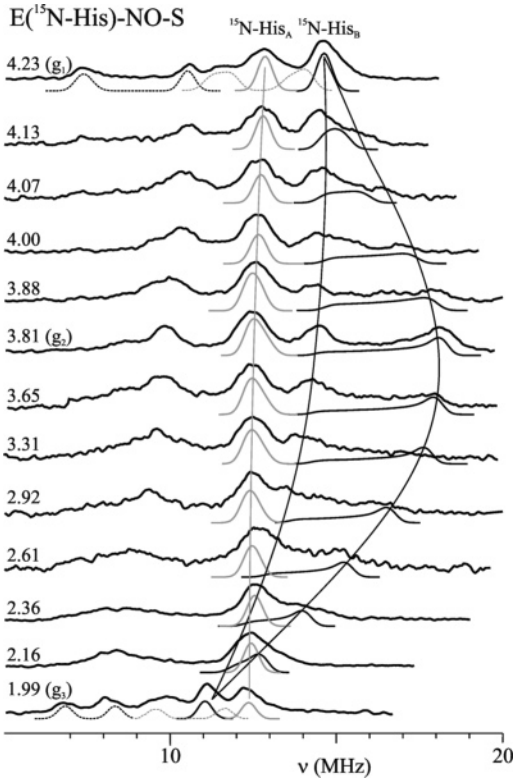

Figure 6. Field-dependent ^{15}N 35 GHz CW ENDOR of **E(^{15}N-His)-NO**−**S**. Fields are as indicated on the plot. Representative simulations, summarized in Table 2, are shown as: gray = ^{15}N-His$_A$, black = ^{15}N-His$_B$.

The remaining ENDOR intensity, below 20 MHz, for **E**(^{15}N-His)-**NO** was attributed above to ν_+(^{14}N) from coordinated NO. The ^{15}N pattern from **E**-(^{15}**NO**) is difficult to follow because its signal is broad and has low-intensity at fields away from g_1 or g_3 (Figure S6). However, the ^{14}NO signal could be followed in spectra from **E**(^{15}N-His**)-NO**, where signals from the coordinated histidines are shifted to higher frequency. The best ^{14}NO simulation is also shown in Figure 5 (dotted lines). Simulation of the ^{15}NO data, while incomplete, agrees satisfactorily with the parameters derived from the fits to ^{14}NO listed in Table 2. The **g** and **A**(NO) tensors are noncoaxial, consistent with bent coordination of NO; the tilt angle, θ = 25°, is equivalent to the anticipated Fe−N−O angle of 155°. The principal hyperfine direction for the NO nitrogen appears then to correspond to the N−O bond direction, rather than the Fe−N bond direction. Overlap and poor resolution precluded an analogous approach to analysis of the ^{14}N-His quadrupole tensors (Figure S6).

E-NO−S/I. Unlike substrate-free **E-NO**, the two histidine nitrogens of **E**(^{15}N-His)-**NO−S** are magnetically distinct at both g_1 and g_3. The best simulation of the 2D pattern for N_A (black line in Figure 6) requires that A_2 and thus the Fe−N_B bond lie along g_2 (Table 2); the parameters for N_B differ little from those for one of the His ligands in **E-NO** (Figure 5). The ^{15}N pattern for the substrate analogue alanine (Figure S7) is similar, which suggests that the substrate amine nitrogen binds trans to the protein-derived histidine ligand, N_B.

The value of $\nu_+(^{15}N_A)$ (∼13 MHz at g_1, Figure 6) appears to change little with field. However, this apparent invariance of $\nu_+(^{15}N)$ reflects a compensating decrease in $\nu_N(^{15}N)$ and an increase in $A'(^{15}N)$. When expressed in terms of the intrinsic hyperfine interaction, there is a small anisotropic term that can be described by an axial contribution with a unique axis along g_3 (see Figure S4A,B); the hyperfine parameters are listed in Table 2, and the resulting simulation is illustrated by the gray line in Figure 6. This indicates that the Fe−N_A bond lies along g_3, placing it trans to the nitrogen of NO.

As is the case for **E-NO**, the field-dependence of the ^{15}N signal from **E**-(^{15}**NO**)**−S** was difficult to follow at fields between g_1 and g_3, while detailed analysis of the ^{14}NO pattern (Figure S8) was prevented by overlap with the signal from ^{14}N of the substrate ACC. The ^{15}NO ENDOR frequencies at g_1 and g_3 are well defined and require that A_3 and g_3 are not coaxial (nonzero θ).

Orientation-Selective ^{17}O ENDOR. Water and E-NO: With decreasing magnetic field, the $H_2{}^{17}O$ resonance seen in Figure 1 shifts to higher frequency (Figure S2) and eventually disappears under the ENDOR signals of ^{1}H (for $g > 3.13$), which are moving to lower field as the g value of observation increases (field decreases). This indicates that $A_1 > 20$ MHz ($A' = (g_1/g_e)A_1 > 40$ MHz). The breadth of the ^{17}O feature also appears to increase at lower fields, which may reflect either an increasing quadrupole coupling at these orientations or the presence of more than one distinct ^{17}O species. Although it is not possible to define the field at which $A(^{17}O)$ maximizes, the observation that $A_{max}(^{17}O)$ does not occur at g_3 indicates that solvent must coordinate in the plane defined by Fe and the two histidine nitrogens, as described earlier.

Carboxylate ^{17}O of I in E-NO−I: The $g_3 = 1.99$ ^{17}O resonance from **E-NO−I**(^{17}O-Ala), seen at $\nu_+ = 12$ MHz of Figure 1A, increases in frequency to $\nu_+ = 17$ MHz at g_2, demonstrating an increase in A' from $A'(g_3) \sim 12$ MHz to $A'(g_2) \sim 26$ MHz (Figure S3), which corresponds to intrinsic ^{17}O-Ala couplings of $A(g_3) \sim 12$ to $A(g_2) \sim 14$ MHz. The ^{17}O signal could not be detected at fields below g_2, which could reflect increased line width due to a large quadrupole coupling or, alternatively, to an even larger hyperfine coupling at g_1, such that the signal becomes undetectable due to overlap with ^{1}H ENDOR signals. With the expectation that the maximal A value will be observed in the direction of the Fe−O bond, the former interpretation suggests that the carboxyl O of ACC lies near the g_2 axis (A_{max} at g_2), while the latter would place the O atom on the g_1 axis. The earlier assessment of the ^{15}N-Ala data, which placed the alanine nitrogen along g_2 and trans to one of the histidyl nitrogens, supports placement of the O atom from substrate/inhibitor along g_1.

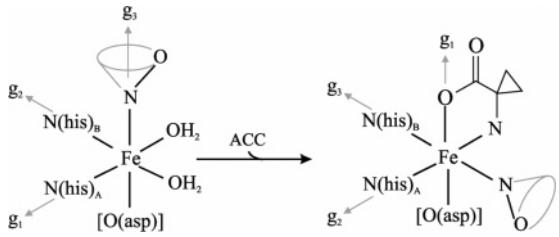

Figure 7. Cartoon depiction of the ACCO−NO Fe(II) binding site, in the absence (left) and presence (right) of substrate ACC, based on the ENDOR results.

Discussion

The results presented here combine CW and pulsed ENDOR techniques in elucidating the composition and structure of the iron(II) active site of ACCO. While well-resolved pulsed ENDOR spectra were obtained in most cases for both **E-NO** and **E-NO−S** at the low-field (g_1) edge of their respective EPR signals, CW ENDOR was required to obtain reliable data at g_3. Similarly, $\nu_+(^{15}NO)$ was not easily observed in Davies-pulsed ENDOR of **E**-(^{15}**NO**)**−S** (Figure 1B), but this feature was readily detected in CW ENDOR of the same sample. Perhaps the most illustrative example of the need to use both techniques is the absence of easily detected exchangeable ^{1}H ENDOR signals in **E-NO** (Figure 1, inset); only when Re-Mims pulsed ENDOR was applied were the ^{2}H signals from coordinated water detected. Analysis of these results provides a picture of the iron active site more detailed than thus far available from other techniques.

Structure of the Fe(II) Active Site in the Presence and Absence of Substrate. The ligand orientations derived from the ENDOR analysis allow us to propose the spatial arrangement of ligand nuclei at the Fe site in ACCO−NO, both with and without bound substrate ACC, shown in Figure 7. The substrate-free, **E-NO** form, on the left, shows a bent Fe−NO unit, with the Fe−N bond lying roughly along g_3. There are two coordinated histidine nitrogens with Fe−N bonds in the plane normal to the Fe−NO bond and cis to one another (N−Fe−N angle ∼90°), as indicated by 2D data for **E**(^{15}N-His)-**NO** (Figure 5); one has Fe−N along the g_1 axis, while the other has Fe−N along g_2. Thus, the ENDOR data (Table 2, Figure 7) strongly support the inclusion of ACCO in the growing family of enzymes that bind Fe(II) with a "2-His-1-carboxylate facial triad." The **E-NO** data show the presence of coordinated solvent. While the number of coordinated solvents cannot be firmly established from the ENDOR data, we favor the model in Figure 7, based on the similarity of the tensor angles derived from the field-dependent data for **E-NO** and **E-NO−S/I**.

In **E-NO−S**, the two histidines retain the cis conformation, with a N−Fe−N angle of ∼90°, but simulations of the data for **E**(^{15}N-His)-**NO−S** (Figure 6, Table 2) suggest that substrate binding causes reorientation of the $[FeNO]^7$ **g** tensor relative to the protein-defined molecular frame. In **E-NO**, the g_1-g_2 plane appears to coincide with the $N_{His}-Fe-N_{His}$ plane, but in **E-NO−S**, the g_2 axis lies along one Fe−N_{His} bond while g_3 lies along the other. Since it is expected that the **g** tensor is defined by the Fe−NO unit in both forms (along g_3), the placement of ^{15}N-His_B along g_3 places it trans to the NO (both His nitrogens were cis to the Fe−NO bond in **E-NO**). This reorientation of **g** and **A** directions in the substrate-bound form then suggests that the NO has physically changed position, as depicted in Figure 7.

Scheme 2

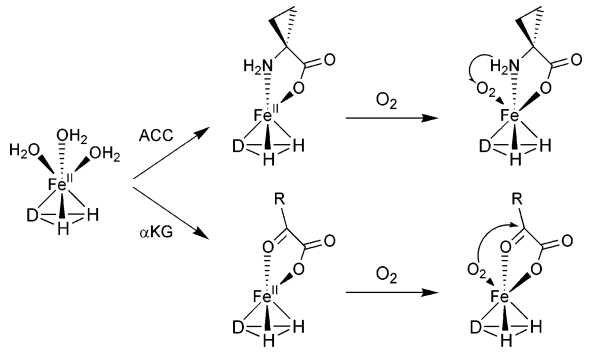

In the absence of substrate, the coordinated NO is free to occupy any of three available coordination positions; two of these coordination sites are taken up by substrate, leaving a single "predetermined" location for the NO and, by analogy, O_2.

Mechanistic Implications. A common mechanistic feature of a number of 2-His-1-carboxylate enzymes is their ability to bind both substrate and O_2 in close proximity, forming a ternary enzyme−substrate−O_2 complex in the committed step to catalysis.[5,21,37] This notion is strongly supported by both spectroscopic and crystallographic evidence on a number of enzymes. The data presented here, showing the simultaneous coordination of two atoms from substrate and one from NO, demonstrate that ACCO follows this mechanistic paradigm, as illustrated in Scheme 2. Furthermore, the data presented here suggest that the orientation of substrate binding is dictated by the protein, which thus determines the orientation of bound O_2.

A longstanding question in the study of the mechanism of ACCO has been the point in the reaction cycle where ascorbate contributes electrons. Initially, it was proposed that ascorbate binds early in the reaction cycle and initiates the reductive activation of oxygen.[38] However, our initial EPR/ENDOR studies showed that NO and ACC bind simultaneously, while ascorbate and NO appeared to be mutually exclusive in the active site.[17] This suggests that a complex of reductant and O_2 with the Fe(II), as seen in the α-ketoglutarate dioxygenases, is an unlikely first step in the reaction. Nevertheless, MCD/CD spectroscopic studies showed that when the activator CO_2 is present, both ACC and ascorbate must bind to the enzyme in order to convert the Fe(II) site from six- to five-coordinate, in preparation for binding of O_2.[24] The current studies clearly show that NO and Ala (or ACC) bind simultaneously to the iron, generating a ternary E−NO−S complex that includes a six-coordinate Fe(II). This makes it unlikely that ascorbate and/or CO_2 bind to the iron in the initial complex of the reaction cycle. Ascorbate may bind to the enzyme and transfer electrons via an outer sphere mechanism. However, the essential role of ascorbate as a reductant early in the reaction is brought into question by our recent transient kinetic studies showing that ethylene can be produced in a single turnover of the enzyme without ascorbate present.[15] Stoichiometric concentrations of ascorbate have been shown to accelerate the reaction significantly, albeit without increasing the yield of ethylene at short times. Ascorbate may therefore serve two roles in the catalytic cycle, acting first as an effector and second as a reductant. The effector role might involve binding at a secondary site far from the active site, accounting for the apparent discrepancy between the CD/MCD results and our earlier EPR/ENDOR results.

The current results support a model in which ACC and O_2 bind simultaneously to the active site and initiate catalysis by an iron-mediated electron-transfer event. CO_2 may bind near the active site and influence the iron environment and reaction chemistry, but it is unlikely that it binds to the iron at the start of the reaction because all of the iron ligation sites are occupied. Once ACC is oxidized to release ethylene and the electrons from this process have been used to reduce O_2, ascorbate may bind and complete the reaction by supplying the second pair of electrons needed to form the 2 equiv of water required by the reaction stoichiometry. Viewed in this way, the role of α-ketoglutarate in the dioxygenase reaction is more directly related to the role of ACC in the ACCO reaction. In both cases, these molecules bind first to the enzyme, and their oxidation results in O−O reduction and possibly bond cleavage. In the dioxygenase case, the resulting activated oxygen species can attack the second substrate to yield hydroxylated product. In the case of ACCO, reduction of the activated oxygen species by ascorbate allows the enzyme to recycle without hydroxylation, as required by the plant host.

Acknowledgment. The authors wish to acknowledge the instrumental talents of Mr. Clark Davoust, the intellectual input of Dr. Peter Doan and Dr. Charles Walsby, and the NIH for funding (HL13531 (B.M.H.), GM 24689 (J.D.L.), and GM 33162 (L.Q.)).

Supporting Information Available: Complete citation for ref 8, a brief description of the simulation procedures and eight figures, including 35 GHz EPR spectra (Figure S1), field-dependent 35 GHz CW ENDOR for **E-NO** in $H_2{}^{17}O$ and $H_2{}^{16}O$ buffers (Figure S2); field-dependent 35 GHz CW and pulsed ENDOR for **E-NO**−**I**(^{17}O-Ala) (Figure S3); theoretical ENDOR spectra for a single ^{15}N interacting with the $E/D = 0.035$ species of **E-NO**−**S**, showing the dependence of the spectra on the parameters (g_{obs}/g_e), θ and ϕ (Figure S4); a comparison of field-dependent 35 GHz CW ENDOR for **E**(^{14,15}N-His)-**NO** and **E**(^{14,15}N-His)-**NO**−**S** (Figure S5); field-dependent 35 GHz CW ENDOR for **E-**(^{14,15}**NO**) (Figure S6); field-dependent 35 GHz CW ENDOR for **E-NO**−**I**(^{14,15}N-Ala) (Figure S7); and field-dependent 35 GHz CW ENDOR for **E-**(^{14,15}**NO**)−**S** (Figure S8) are presented. This material is available free of charge via the Internet at http://pubs.acs.org.

JA0500862

(37) Solomon, E. I.; Decker, A.; Lehnert, N. *Proc. Natl. Acad. Sci. U.S.A.* **2003**, *100*, 3589−3594.
(38) McRae, D. G.; Baker, J. E.; Thompson, J. E. *Plant Cell Physiol.* **1982**, *23*, 375−383.